RSC Advances

ROYAL SOCIETY OF CHEMISTRY

www.rsc.org/advances

Influence of Earth-Abundant bimetallic (Fe-Ni) nanoparticles embedded CNFs as a Low Cost Counter Electrode Material for Dye-Sensitized Solar Cell

K. Saranya[a], A. Subramania[a], N. Sivasankar[b]

a. Electrochemical Energy Research Lab, Centre for Nanoscience and Technology,
Pondicherry University, Puducherry - 605 014, India.

b. Department of Metallurgical Engineering & Materials Science,
Indian Institute of Technology-Bombay, Mumbai, India-400076

*Corresponding Author E-mail: a.subramania@gmail.com
*Phone: +91413 2654980, Fax: +91413 2655348.

ABSTRACT

Earth-abundant bimetallic (Fe-Ni) nanoparticles embedded carbon nanofibers (CNFs) have been prepared by electrospinning technique and used as counter electrode (CE) material for dye-sensitized solar cells (DSSC). The structural and morphological properties were explored by X-ray diffraction (XRD), Raman spectroscopy, Field-emission scanning microscope (FE-SEM) and Transmission electron microscope (TEM) studies. The results of cyclic voltammetry (CV), electrochemical impedance and Tafel polarization studies revealed that (Fe-Ni)-CNFs demonstrated superior electrocatalytic activity, electrochemical stability, low charge transfer resistance (R_{ct}) and high exchange current density for the reduction of triiodide (I_3^-). Furthermore, it was observed that the DSSC fabricated using (Fe-Ni)-CNFs as counter electrode had achieved almost comparable power conversion efficiency (PCE) than the same fabricated using std. Pt. This is due to large surface area and randomly oriented interconnected porous morphology with graphitized structure of the prepared CNFs, which enhanced the contact of a large quantity of ionic liquid electrolyte that leads to a faster redox kinetics of I_3^-/I^-. It revealed that (Fe-Ni)-CNFs could be used as a low cost and an efficient counter electrode material for DSSCs.

Keywords: Dye-sensitized solar cell, Carbon nanofibers, Counter electrode, Bimetallic nanoparticles embedded carbon nanofibers.

Introduction

The abundant solar energy and photovoltaic devices acquire more attention to compensate the energy demand due to the depletion of fossil fuels. Dye-sensitized solar cell, which belongs to the third generation solar cells has been considered as an effective alternate for the conventional p-n junction solar cells. It has the advantages of simple fabrication procedure, good plasticity and environmental friendliness. The first DSSC was reported in 1991 at Ecole Polytechnique Federale Lausanne (EPFL) by Gratzel et al.[1] Normally, DSSC comprises a monolayer of dye adsorbed wide band gap n-type TiO_2 semiconductor on transparent conductive oxide substrate (TCO) as photoanode, I^-/I_3^- redox couple in an organic solvent as electrolyte and Pt as counter electrode.[2] Till date, the maximum efficiency achieved is 13%.[3] Hence, further steps have been taken to increase the efficiency of DSSC by improving the performance of its components. Among the components of DSSC, CE plays a main role for the completion of electrical circuit and also for the regeneration of iodide from triiodide through reduction process. Pt is employed as a counter electrode due to its high electrocatalytic activity and conductivity. However, it has some drawbacks such as expensiveness, rarity, low surface area and instability with the redox couple which limits the longtime operation due to the formation of PtI_4.[4] By developing cost effective earth abundant CE materials, the energy conversion cost will be reduced to \$0.4/W_P.[5] Therefore, several research efforts are in progress to develop the alternative low cost materials with high conductivity, good electrocatalytic activity and electrochemical stability; this could help the commercialization of DSSCs.

Various carbon materials, conducting polymers, sulfides, nitrides, carbides and also their composites have been reported as CE materials in place of Pt.[6-11] Especially, carbonaceous materials such as carbon black, graphite, graphene, carbon nanotubes and carbon nanofibers are considered as good alternative CEs to replace Pt, as they possess high conductivity and electrochemical stability against I_3^-/I^-.[12, 13] Among them, one-dimensional CNFs are received broad interest as electrode materials in electrochemical energy devices including supercapacitors, hydrogen storage and batteries due to their large specific surface area, good conductivity, tensile strength and various packing arrangements of graphene sheets (i.e. tubular, herringbone and lamellar structure).[14] Primarily, CNFs prepared from polyacrylonitrile (PAN) by electrospinning technique, followed by its stabilization and carbonization process.[15, 16] The preparation method is another essential feature in the development of electrocatalysts as well as electrodes along with the chemical and electrochemical nature of the materials. In addition, recently the electrospun one-dimensional nanofibers and composite nanofibers are widely used for several applications such as photovoltaics, photocatalysis and energy storage devices.[17-20] Qiao et al. reported CNFs as counter electrode for DSSCs, which has lower photovoltaic performance when compared to platinum due to its poor electrocatalytic activity.[21] This can be improved significantly by enhancing its active surface area by making it as highly porous CNFs as well as CNFs based composites, which is beneficial to one dimensional conducting pathway for I^-/I_3^- ions. Furthermore, the synergistic effect of CNFs based composite enhanced the electrical conductivity and more catalytic active sites for I_3^- reduction that results in low charge transfer resistance.[13] Recently, a very few CNFs based composites such as CNF-TiO_2,[22] Ni-CNT-CNFs,[23] TiC-CNFs-Pt,[24] Pd-Co doped CNFs [25] and Ni-Cu incorporated CNFs [26] have been prepared by electrospinning technique and used as CEs for DSSCs. But, it is observed that the achieved PCE of CNFs based CEs is ~4% lower than std. Pt. Therefore, further research is being done to enhance the photovoltaic performance of CNFs based composites. Bimetallic nanoparticles (NPs) of a first-row transition metals have composition-dependent optical, magnetic, and catalytic properties compared to single metal nanoparticles.[27] Iron and nickel are the most abundant elements on earth. Furthermore, the design of catalysts in which Fe is alloyed with a second metal possesses remarkably enhanced electrocatalytic activity due to the possible variation of geometric and electronic properties of the active sites. Bimetallic Fe-Ni is utilized as an electrocatalyst for various applications.[28, 29] Moreover, till date it is observed that there is no report on the use of bimetallic Fe-Ni nanoparticles embedded CNFs as CE for DSSCs.

In the present investigation, bimetallic Fe-Ni nanoparticles embedded CNFs have been prepared by a simple electrospinning technique and its electrochemical and photovoltaic performance are investigated in detail to use as a newer and low cost CE in DSSCs.

Experimental

Preparation of Fe-Ni embedded CNFs

Polyacrylonitrile was dissolved in N, N-dimethylformamide to prepare 10 wt. % solution. To this, 0.188 g of Ni acetate and 0.271 g of Fe nitrate were added and the solution was allowed for stirring about 12 h. This solution was filled into 15 ml plastic syringe equipped with a 27 gauge needle. The electrospinning was carried out at high voltage of 25 kV using a high voltage DC power supply. The flow rate and distance between spinneret to collector were maintained as 0.5 ml h^{-1} and 15 cm, respectively. The electrospun mat was first stabilized at the temperature of 250 °C for 2 h in air followed by carbonization was done at 1200 °C with the heating rate of 2 °C for

2 h in nitrogen atmosphere to get bimetallic Fe-Ni nanoparticles embedded CNFs. The same procedure was adopted to prepare pure CNFs without the addition of metal precursors.

Physical and Electrochemical Characterization

The phase purity of CNFs and Fe-Ni embedded CNFs were confirmed by X-ray diffraction studies (Rigaku, Model: Ultima IV). The graphitic nature and microstructure of carbonaceous materials were determined using confocal micro-Raman spectrometer with a laser beam of 514 nm (Renishaw, Model: RM 2000). The surface morphology of bimetallic Fe-Ni embedded CNFs was analyzed by FE-SEM (JSM, JEOL 7600F). The presence of Fe and Ni embedded onto the CNFs was observed by energy dispersive X-ray analysis (EDX) and energy dispersive spectroscopy (EDS) equipped with FE-SEM. The inclusion of Fe-Ni and graphitic phase in CNFs and its crystallinity was identified by TEM and SAED studies (Philips, Model: CM 200). The surface area of CNFs and Fe-Ni embedded CNFs were evaluated using surface area analyzer (Smart instruments, Model: Smart Sorb 92/93). The cyclic voltammetry study was carried out by electrochemical workstation (VSP, Bio-Logic, France) using a three-electrode cell configuration to explore the electrocatalytic activity of CEs towards the reduction of I_3^- ion in the redox electrolyte. This three-electrode cell consists of the prepared CE material with an active area of 0.25 cm^2 as working electrode, Pt with an active area of 1 cm^2 as counter electrode and Ag/AgCl as the reference electrode. 0.01 M LiI, 0.001 M I_2 and 0.1 M $LiClO_4$ in acetonitrile was used as an electrolyte in the potential range of -1.0 to 1.0 V at different scan rates. The electrochemical impedance measurement was performed for std. Pt, CNFs and (Fe-Ni) embedded CNFs electrodes by fabricating symmetric cells. The surlyn tape was sandwiched between two symmetrical electrodes as the spacer to find out the charge transfer resistance in the frequency range of 100 KHz to 1 mHz. The Tafel polarization measurements were done at the scan rate of 50 mV s^{-1} to verify the electrocatalytic activity of the CE using the same symmetrical cells.

Fabrication of DSSCs

The ITO glass plates were washed with acetone, ethanol and deionized water in ultrasonic water bath and then the plates were dried in air. The ITO glass plates were chosen for their low surface roughness and higher transmittance compared to FTO glass plates.[30] A scotch tape was used as a spacer to control the film thickness. The TiO_2 paste (Dyesol Ltd) was coated on the conducting glass substrate between the scotch tape by doctor blade technique and it was sintered at 450 °C for 30 min. The thickness and area of the photoanode films were found to be about 12 μm and 0.20 cm^2, respectively. The sintered photoanode was dipped into a solution containing 3×10^{-4} M of dye, Di-tetrabutyl ammonium cis-bis(isothiocyanato) bis (2,2'-bipyridyl-4,4'-dicarboxylato) Ruthenium(II) for 24 h. After dye adsorption, dye-sensitized TiO_2 photoanodes were washed with anhydrous ethanol so as to remove excess dye and left to dry in air.[31] The different counter electrodes were prepared by mixing 35 wt. % of each prepared CE material (CNFs and Fe-Ni embedded CNFs) mixed with 15 wt. % of ethyl cellulose (binder). Subsequently, they were dispersed in 50 wt. % of terpineol and then stirred by intermittent sonication. This paste was coated on pre-cleaned ITO plate by doctor blade technique with the thickness of 15 μm and then were dried for 30 min. at 300 °C.

The DSSCs were assembled using TiO_2 photoanode with various counter electrodes such as std. Pt paste (Dyesol Ltd.), CNFs and Fe-Ni embedded CNFs individually by a hot press at 110 °C. The I^-/I_3^- redox mediator which contains 0.5 M of LiI, 0.05 M of I_2,0.5 M of TBP and 0.5 M of 1-butyl-3-methylimidazolium iodide (ionic liquid) in acetonitrile was injected into the cells via two small holes drilled on the CE side. Finally, the holes were sealed with the aid of small squares of surlyn tape. [32]

The photovoltaic performance of the assembled DSSCs was carried out using a calibrated AM 1.5 solar simulator (Newport, Oriel instruments USA 150W, model: 67005) with a light intensity of 100 mW cm^{-2} and a computer-controlled digital source meter (Keithley, Model: 2420). The PCE (η) of the assembled cells was calculated from the measured photovoltaic parameters such as fill factor (FF), open circuit voltage (V_{oc}), short circuit current density (J_{sc}) and incident optical power (P_{in}). We fabricated three DSSCs for each system and their photovoltaic performance values were measured and average values were taken.

Results and discussion

XRD Studies

Phase purities of the prepared CNFs and Fe-Ni embedded CNFs which were confirmed by XRD patterns are shown in Fig. 1. The characteristic peak at 25.4° is indexed as the graphitic structure of CNFs. Furthermore, the diffraction peaks at 43.5°(111), 50.3° (200) and 75.4° (220) are attributed to the characteristic reflections of the face centered cubic (fcc) Fe-Ni alloy nanoparticles (JCPDS 47-1417).[33] There is no individual Fe or Ni nanoparticles formed during the carbonization.

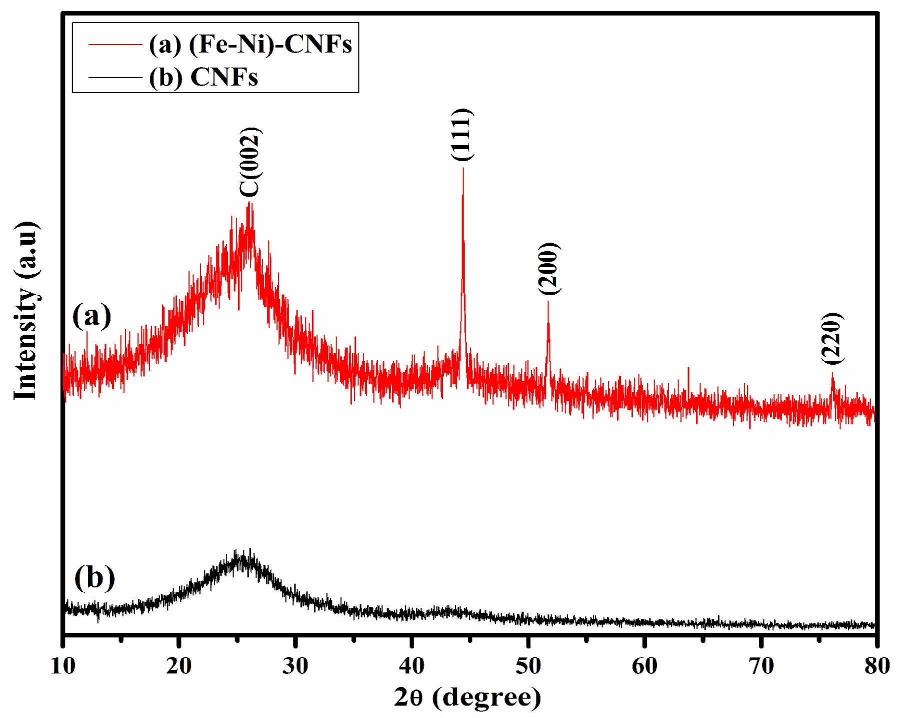

Fig. 1 XRD patterns of CNFs and Fe-Ni embedded CNFs carbonized at 1200 °C for 2 h in N_2 atmosphere.

Raman spectral studies

Fig.2 shows the Raman spectra of CNFs and Fe-Ni embedded CNFs which consist of two characteristic peaks at 1350 cm^{-1} and 1580 cm^{-1} representing the defect induced mode A_{1g} or D band and the ordered E_{2g} mode or G band. The G-band is associated with the (002) diffraction peak of XRD pattern. R value (I_D/I_G) of CNFs and Fe-Ni embedded CNFs are 1.04 and 0.69, respectively. The lower D/G intensity ratio of Fe-Ni-CNFs suggesting the graphitization, larger surface area and porous nature of the carbonaceous material is attributed to the high catalytic ability of Fe-Ni alloy nanoparticles towards carbonization.[34, 35] These properties Fe-Ni embedded CNFs may facilitate the fast electron transfer kinetics at the CE electrode/electrolyte interface.[36, 37]

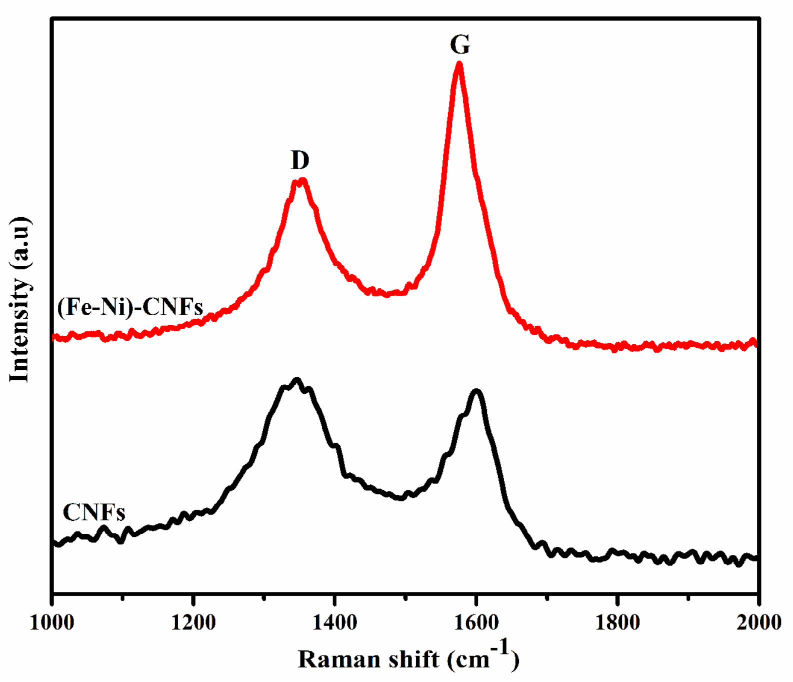

Fig. 2 Raman spectra of CNFs and Fe-Ni embedded CNFs carbonized at 1200 °C for 2 h in N_2 atmosphere.

FE-SEM studies

The FE-SEM morphologies of Fe-Ni embedded CNFs before and after carbonization are shown in Fig. 3 (a&b). FE-SEM image of Fe-Ni embedded CNFs before carbonization indicates that the fibers are continuous and beads-free morphology. Fe-Ni embedded CNFs after carbonization exhibits randomly oriented interconnected porous morphology and the well embedded bimetallic Fe-Ni nanoparticles in the CNFs. The average diameter of Fe-Ni embedded CNFs before and after carbonization are ~340 nm and ~230 nm, respectively. Further, the surface area of Fe-Ni embedded CNFs was has been calculated by using Brunauer-Emmett-Teller (BET) surface area measurement that shows 240 m^2 g^{-1} which is much higher than the CNFs (94 m^2 g^{-1}). The presence of Fe-Ni alloy nanoparticles create more randomly oriented interconnected pores in CNFs is due to the dissolution-precipitation mechanism during catalytic graphitization that leads to large surface area of CNFs.[38] The larger surface area is essential for high electrocatalytic activity. Further, this highly porous structure with larger surface area will enhance the diffusion of I^-/I_3^- redox species.[39]

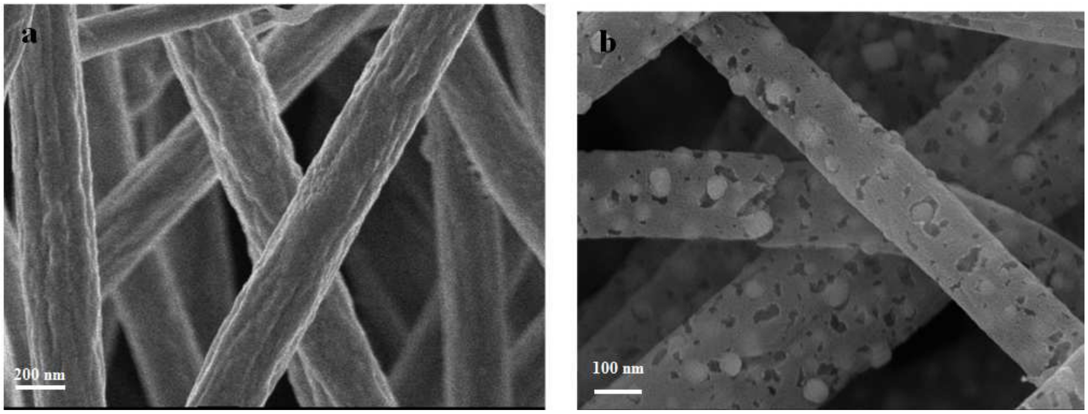

Fig. 3 (a) FE-SEM image of Fe-Ni embedded CNFs before carbonization, (b) FE-SEM image of Fe-Ni embedded CNFs after carbonization at 1200 ˚C for 2 h in N_2 atmosphere.

TEM studies

The presence of bimetallic Fe-Ni nanoparticles on CNFs and the crystallinity of CNFs further examined by TEM analysis. It can be seen that the bimetallic Fe-Ni alloy nanoparticles are well embedded in the CNFs. Fe-Ni embedded CNFs consists of both turbostratic amorphous phase and ordered graphitic phase [Fig. 4 (a-c)]. The porous and graphitic nature of CNFs provides large number of electrocatalytic active site for I_3^- reduction. The selected area electron diffraction (SAED) pattern exhibits bright diffraction spots indicated the formation of crystallinity of composite nanofibers [Fig.4 (d)]. The obtained SAED pattern matches with the results of XRD pattern. The elemental distribution of Fe-Ni embedded CNFs was examined by TEM-EDX and EDX-line analysis pattern [Fig.4 (e &f)]. Furthermore, EDS images of Fe-Ni embedded CNFs are shown the presence of Carbon, Fe and Ni, which are represented by red, green and blue regions, respectively [Fig. 3(g)]. It confirms the distribution of bimetallic Fe-Ni nanoparticles in CNFs.

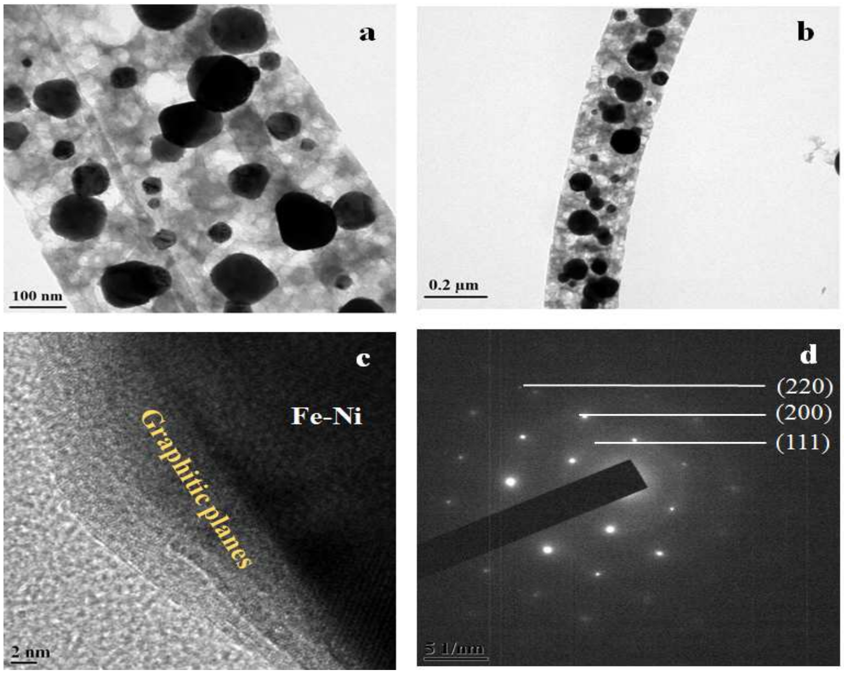

Fig. 4 (a&b) TEM image of Fe-Ni embedded CNFs after carbonization at different magnifications, (c) TEM image of graphitic and Fe-Ni planes in CNFs and (d) SAED pattern of Fe-Ni embedded CNFs.

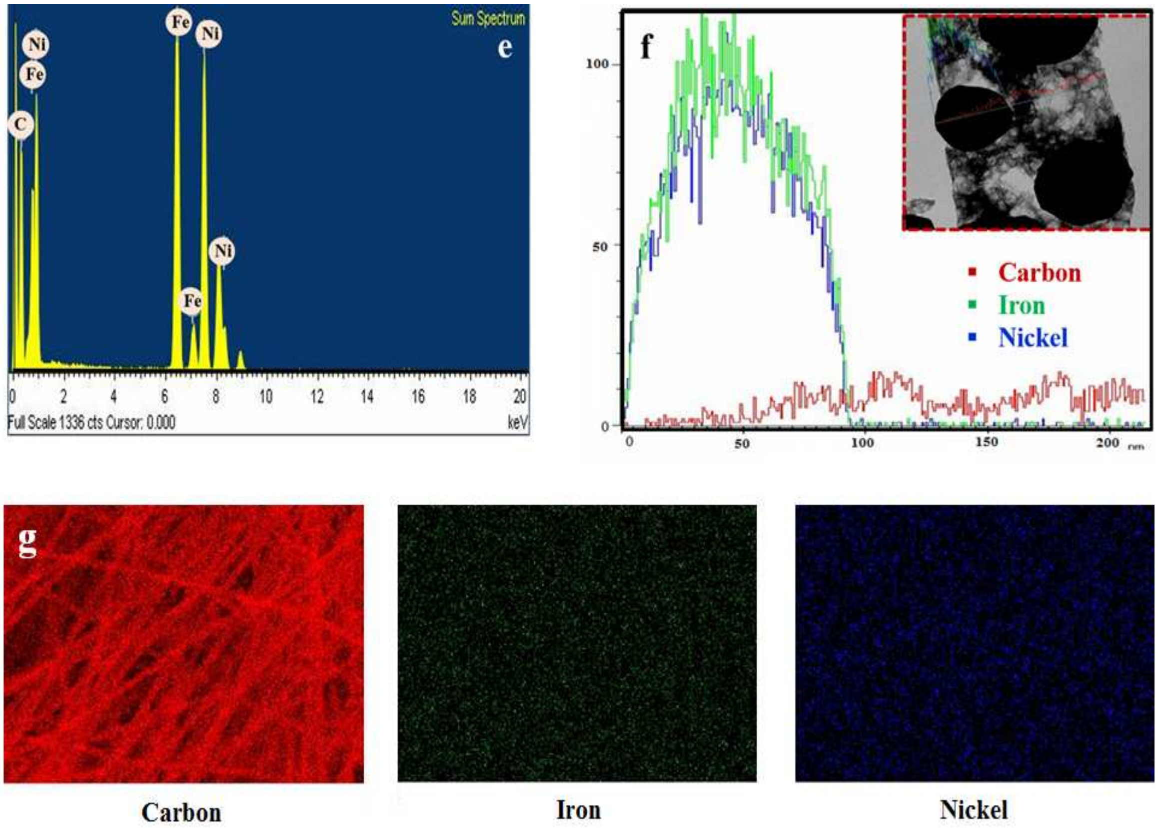

Fig. 4 (e) TEM-EDX analysis (f) Line analysis of Fe-Ni embedded CNFs after carbonization at 1200 ˚C for 2 h in N_2 atmosphere, (g) EDS elemental mapping images of Fe-Ni embedded CNFs.

Electrochemical Studies

Electrochemical behaviors of Fe-Ni embedded CNFs electrode were evaluated using cyclic voltammetry, electrochemical impedance and Tafel polarization studies and their results are compared with CNFs and std. Pt electrodes.

Cyclic Voltammetry Studies

Cyclic voltammetry is widely used to study the redox processes and the kinetics of electron transfer reactions. The cyclic voltammograms were carried out to evaluate the electrocatalytic activity of the counter materials such as std. Pt, CNFs and Fe-Ni embedded CNFs. The obtained cyclic voltammograms for std. Pt, CNFs and Fe-Ni embedded CNFs are shown in Fig. 5 (a). It can be seen that each cyclic voltammogram consists of a pair of oxidation (anodic peak) and reduction (cathodic peak) peaks. Among them, the left pair of redox peaks directly influenced the photovoltaic performance of DSSC. The right pair of redox peaks has no significant impact on DSSCs.[40] It can also be observed that the Fe-Ni embedded CNFs possess higher magnitude of redox peak current intensity and larger electrochemical active surface area. The larger electrochemical active surface area of the electrode is due to the larger enclosed redox reaction area of the CV curve. [7] Furthermore, the cathodic peak potential of Fe-Ni embedded CNFs is more positive than CNFs and also comparable to std. Pt. It indicates the lower overpotential losses, improved electrocatalytic activity and fast electron transfer kinetics in the reduction of triiodide ions. The improved electrocatalytic activity is due to the addition of bimetallic Fe-Ni nanoparticles act as an effective catalyst for the growth of CNFs, which increased the graphitic nature as well as the surface area.

$$3I^- \rightleftharpoons I_3^- + 2e^- \quad \text{Oxidation} \qquad (1)$$

$$I_3^- + 2e^- \rightleftharpoons 3I^- \quad \text{Reduction} \qquad (2)$$

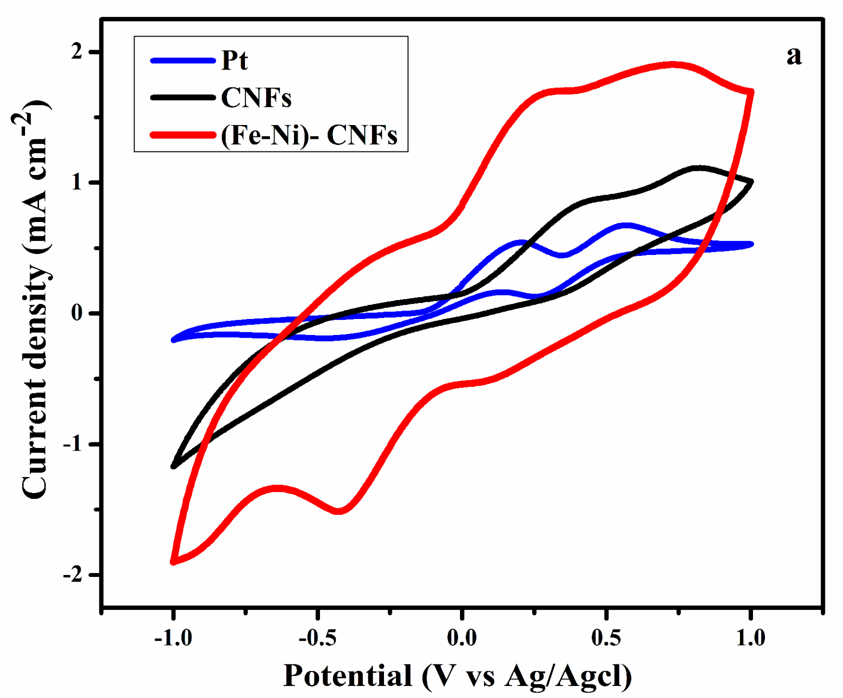

Fig. 5 (a) Cyclic voltammograms of Pt, CNFs and Fe-Ni embedded CNFs in an liquid electrolyte containing a mixture of 0.01 M LiI, 0.001 M I_2 and 0.1 M $LiClO_4$ in acetonitrile at the scan rate of 50 mV s^{-1}.

The CVs was done at various scan rates for std. Pt, CNFs and Fe-Ni embedded CNFs are shown in Fig. 5 (b). As expected, the peak current density varied linearly with different scan rates. The reduction peaks (J_{red}) shift linearly to the negative side and the corresponding oxidation peaks shift (J_{ox}) to the positive side with increasing scan rates. A relationship between both the oxidation and reduction peak currents and the square root of different scan rates is shown in Fig. 5 (c). The linear relationship at different scan rates suggests that the oxidation and reduction reactions of I_3^-/I^- are diffusion limited which obeys the Randles-Sevcik equation (eqn.3).[41]

$$J_{red} = Kn^{1.5} AC\,(D_n)^{0.5}\,\upsilon^{0.5} \qquad (3)$$

where, K is the constant of 2.69×10^5, n is 2 since two electrons involved in the electrochemical reduction reaction, A is the area of the working electrode (cm^2), C represents the bulk concentration of I_3^- species ($mol\ L^{-1}$) , D_n is the diffusion constant ($cm^{-2}\ s^{-1}$) and υ is the scan rate ($mV\ s^{-1}$). The value J_{red} is higher for Fe-Ni embedded CNFs than std. Pt and CNFs which could enhance the charge transfer and diffusion of iodide species. Further, the cyclic voltammetry was carried out for 100 consecutive cycles at the scan rate of 50 $mV\ s^{-1}$ to verify compatibility of Fe-Ni embedded CNFs with the electrolyte for long time utility is shown in Fig. 5 (d). The relationship between number of cycles and maximum reduction peak current densities is shown in Fig. 5 (e). Unexpectedly, it is observed that there is only trivial variation in the maximum J_{red} between 1st and 100th cycle indicating an excellent electrochemical stability of Fe-Ni embedded CNFs electrode with the electrolyte.[42, 43] CV analysis of Fe-Ni embedded CNFs revealed both promising electrocatalytic activity and electrochemical stability with the redox electrolyte, hence, it can be exploited as an effective CE for DSSC in place of Pt.

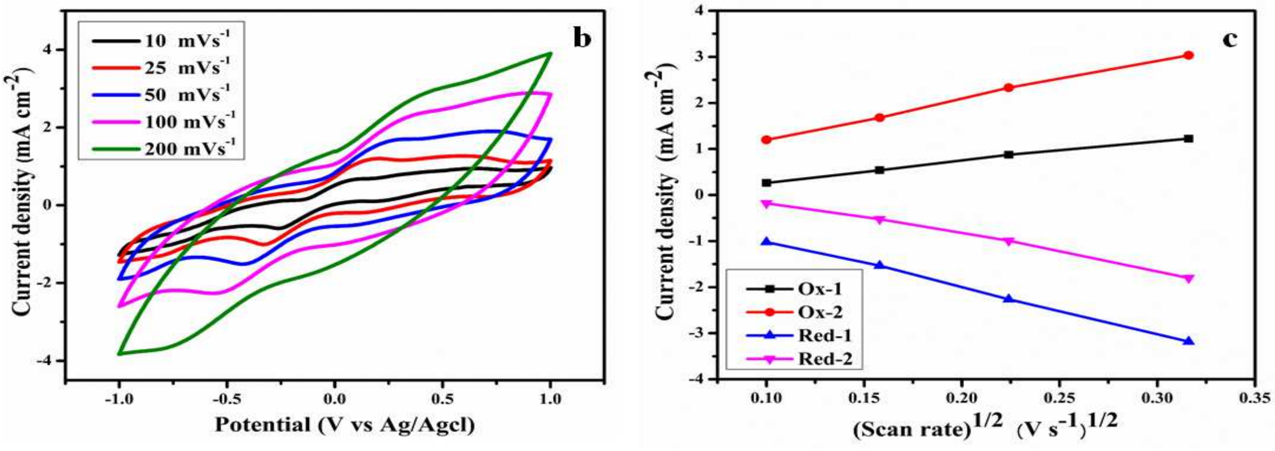

Fig. 5 (b) Cyclic voltammograms of Fe-Ni embedded CNFs at different scan rates of 10, 25, 50,100 and 200 $mV\ s^{-1}$, (c) The oxidation and reduction current densities of Fe-Ni embedded CNFs electrode vs Square root of different scan rates.

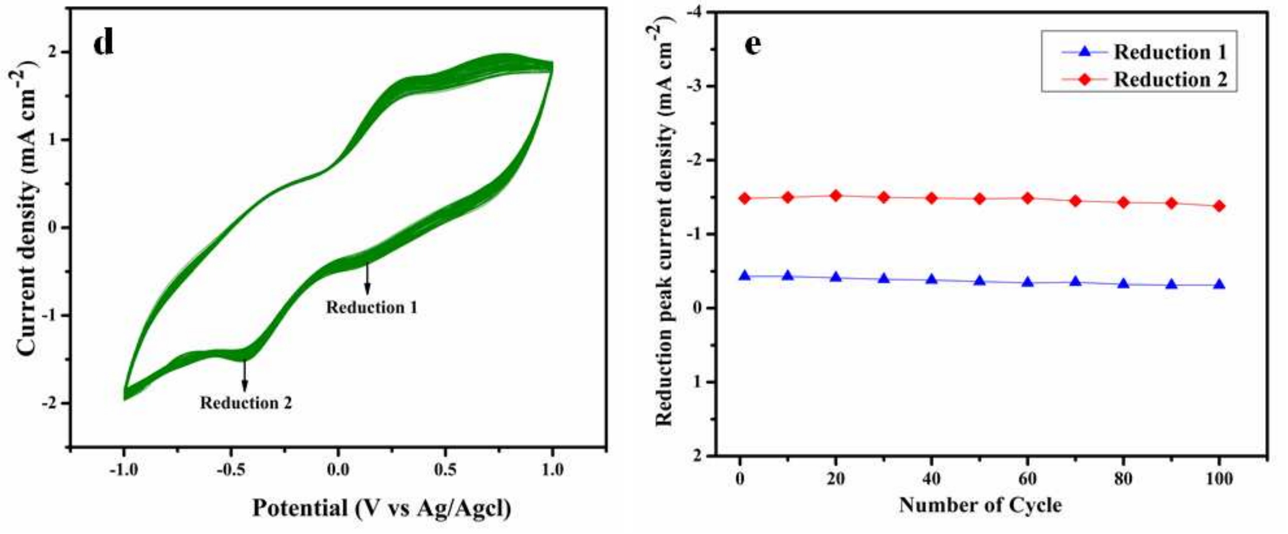

Fig. 5 (d) Cyclic voltammograms of Fe-Ni embedded CNFs for 100 consecutive cycles at the scan rate of 50 mV s^{-1}, (e) The relationship between number of cycles and the maximum reduction peak current density for Fe-Ni embedded CNFs.

EIS Studies

Electrochemical impedance spectroscopy is an additional tool to investigate charge transfer kinetics of an electrochemical system. The Nyquist plots of std. Pt, CNFs and Fe-Ni embedded CNFs were compared with the corresponding Randles-type equivalent circuit is shown in Fig. 6. The equivalent circuit is shown as inset and the parameters were determined from Z-fit software. The Nyquist plots contains series resistance (R_s) represents the resistance of substrate in the higher frequency region and charge transfer resistance at the electrode-electrolyte interface and Nernst diffusion impedance (Z_W) in the lower frequency region.[22, 24] The EIS parameters such as series resistance and charge transfer resistance were calculated from the Nyquist plots are summarized in Table 1. The series resistance of CNFs electrode was about twice to that of Pt electrode. This is probably caused by the high thickness (~15 μm) of the CNFs electrode and higher electronic conductivity of the Pt which are consistent with previous reports.[44] Furthermore, R_s value of Fe-Ni embedded CNFs is reduced due to graphitic character of CNFs will provide sufficient electrical conductivity that leads to better contact with the substrate. The value of R_{ct} determines the electrocatalytic activity of the electrode. It can be observed that R_{ct} value of Fe-Ni embedded CNFs (3.01 Ω) is slightly lower than std. Pt (3.12 Ω).[45, 46] This might be attributed to the large surface area, randomly interconnected porous morphology with graphitized structure by the addition of Fe-Ni nanoparticles in CNFs when compared to std. Pt. It enhanced the electrocatalytic activity and reduce overpotential of Fe-Ni embedded CNFs for the reduction of I_3^- which is evident from the cyclic voltammograms (Fig.5a). In addition, the addition of bimetallic Fe-Ni nanoparticles in CNFs improved the contact with substrate compared to pure CNFs. The porous network enhances the contact of a large quantity of ionic liquid electrolyte that leads to a faster redox reaction kinetics of I_3^-/I^-.[45]

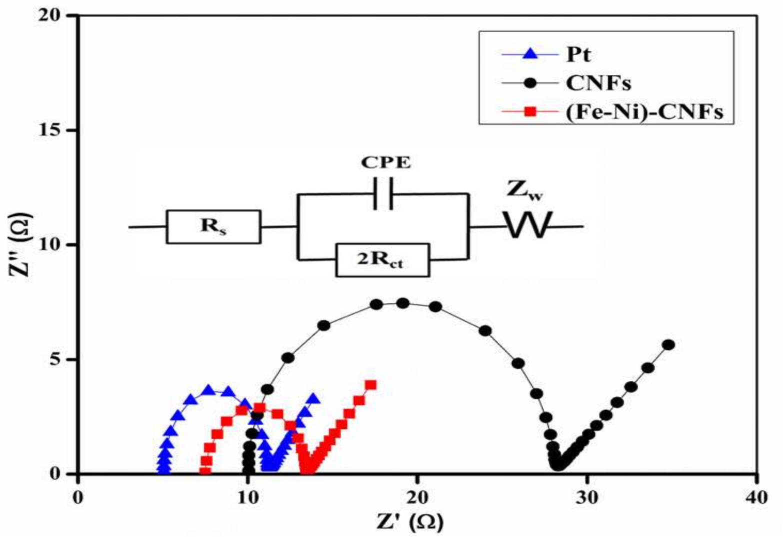

Fig. 6 Nyquist plots of symmetrical cells fabricated with two identical std. Pt, CNFs and Fe-Ni embedded CNFs electrodes.

Table 1 Electrochemical parameters derived from Nyquist and Tafel plots for various counter electrode materials.

Electrodes	**R_s (Ω)**	**R_{ct} (Ω)**	**J_0 (mA cm^{-2})**
Pt (Std)	5.07	3.12	4.12
CNFs	10.06	9.12	1.41
(Fe-Ni)-CNFs	7.50	3.01	4.26

Tafel polarization studies

Tafel polarization curves were also carried out to verify further the electrocatalytic activity using the same symmetrical cells. The Tafel plot comprises of three regions. The curve at high potential (horizontal part) is attributed to the diffusion zone, at low potential region is ascribed to the polarization zone and the curve at middle potential (with a sharp slope) is represented as Tafel zone (potential region higher than 120 mV) related to charge transfer between triiodide and the CE. In theory, the charge-transfer resistance is inversely varies with exchange current density (J_0), where R and F are constant, T is the room temperature and n is the number of electrons involved in the reduction reaction [eqn. (4)]. The J_0 value can be estimated from an intersection of tangent line of the Tafel zone and the extension line of the zero bias, then the large slope of Tafel zone tangent line will lead to a large J_0 and small R_{ct}. The electrocatalytic activity of the material depends on the J_0 and limiting diffusion current density (J_{lim}).[42, 47] The cathodic branch of the curve exhibits a large slope in the Tafel zone that indicates a high J_0 for Fe-Ni embedded CNFs than CNFs signifying better catalytic performance [Fig. 7]. The J_0 can be also calculated using the eqn. (4) and their values are given in Table 1. The Tafel polarization measurement result is in good agreement with EIS results.

$$J_0 = RT / nFR_{ct} \qquad (4)$$

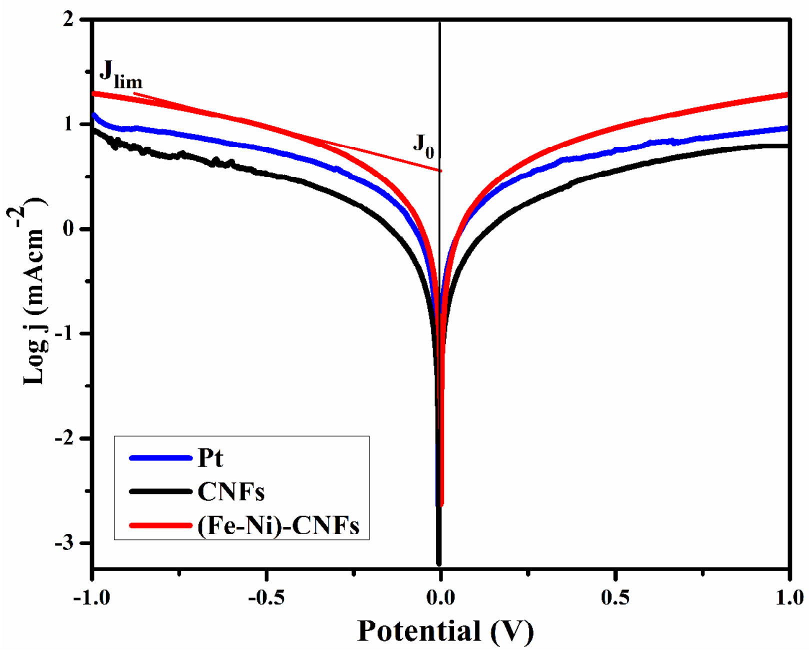

Fig. 7 Tafel plots for std. Pt, CNFs and Fe-Ni embedded CNFs counter electrode materials at the scan rate of 50 mV s^{-1} using the symmetric cells.

Photovoltaic performance studies

The photovoltaic performance for DSSCs fabricated using separately Fe-Ni embedded CNFs, std. Pt and CNFs as CEs are shown in Fig. 8. Their corresponding photovoltaic parameters are summarized in Table 2. The DSSC based on Fe-Ni embedded CNFs achieved almost comparable PCE than std. Pt. However, it is higher than other previously reported systems (Table 3). The CNFs based DSSCs has lesser fill factor (FF) compared to Pt based DSSC which has high R_s due to thick CNFs layer. The inclusion of bimetallic nanoparticles have reduced the total series resistance of Fe-Ni embedded CNFs based DSSC which facilitate the improvement of FF than CNFs based DSSC. The open circuit voltage (V_{oc}) of Fe-Ni embedded CNFs was higher compared to the std. Pt based DSSC is attributed to the superior electrocatalytic activity of Fe-Ni embedded CNFs based CE.[48-50] Therefore, the overall improvement on the photovoltaic performance of Fe-Ni embedded CNFs based DSSC is due to the large surface area and randomly oriented interconnected porous morphology with graphitized structure that facilitate high electrocatalytic activity, low charge transfer resistance at the electrode/electrolyte interface and fast reaction kinetics for the reduction of I_3^- to I^-.

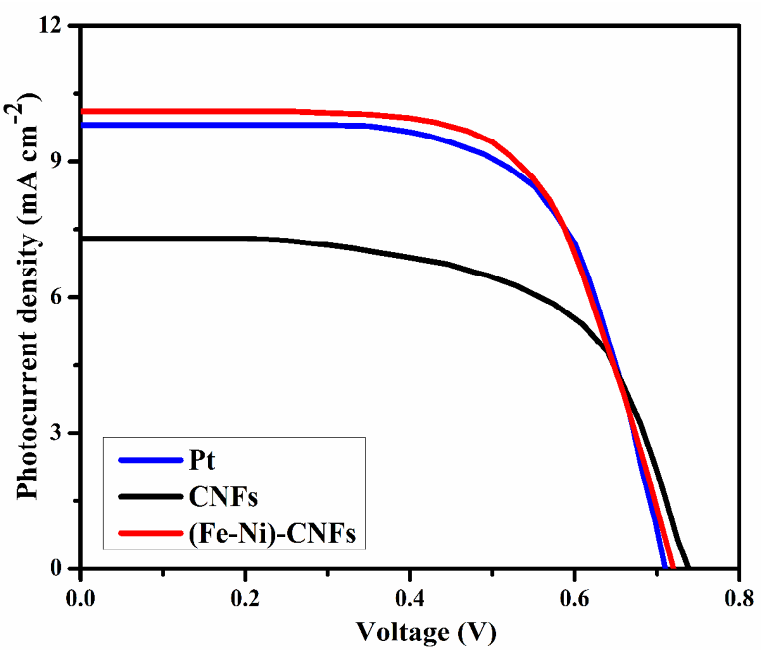

Fig. 8 Photovoltaic performance of DSSCs fabricated using different CEs in a calibrated AM 1.5 solar simulator with a light intensity of 100 mW cm^{-2}.

Table 2 Photovoltaic parameters of DSSC fabricated using different counter electrode.

Counter Electrodes	V_{oc} (V)	J_{sc} (mA/cm^2)	FF	η (%)
Pt (Std)	0.71	9.8	0.66	4.6
CNFs	0.74	7.3	0.58	3.1
(Fe-Ni)- CNFs	0.72	10.1	0.65	4.7

Table 3 Comparison of photovoltaic performances of DSSCs fabricated using CNFs based composite as counter electrodes.

Counter Electrode	V_{oc} (V)	J_{sc} (mA cm^{-2})	FF	Cell Efficiency, η (%)		Achieved PCE w.r.t Std. Pt (%)	Ref
				Std. Pt	CNFs composites		
CNFs	0.76	12.60	0.57	6.97	5.50	78.9	[21]
CNFs/TiO_2	0.84	13.69	0.63	7.57	7.46	95.8	[22]
Ni-CNT-CNFs	0.80	15.83	0.63	8.32	7.96	95.7	[23]
TiC/CNFs-Pt	0.78	14.40	0.64	7.54	7.21	95.6	[24]
(Pd-Co) in CNFs	0.71	9.80	0.37	-	2.50	-	[25]
Ni-Cu in CNFs	0.70	7.67	0.65	5.60	3.50	62.5	[26]
(Fe-Ni) in CNFs	0.72	10.10	0.65	4.60	4.70	~102.2	This work

Conclusion

The electrospinning technique was employed to prepare Fe-Ni embedded CNFs effectively. XRD results confirms that the formation of Fe-Ni alloy nanoparticles embedded CNFs. The inclusion of Fe and Ni in CNFs and an average diameter (~230 nm) of nanofibers were identified from FE-SEM images. The TEM results confirmed that CNFs was embedded with polycrystalline Fe-Ni nanoparticles. The superior electrocatalytic activity of Fe-Ni embedded CNFs was confirmed from the outcomes of CV, EIS and Tafel polarization studies. The photovoltaic performance of DSSC fabricated using Fe-Ni embedded CNFs as counter electrode exhibited that the V_{oc}, J_{sc}, FF and PCE are 0.72 V, 10.1 mA cm^{-2}, 0.65 and 4.7%, respectively. The Fe-Ni embedded CNFs based DSSC achieved almost comparable PCE than the same fabricated using std. Pt was due to enhanced electrocatalytic activity, electrochemical stability, charge transfer rate and faster reaction kinetics with high exchange current density. Therefore, the proposed outcomes highlighted the promising CE material performance of Fe-Ni embedded CNFs. Hence, it could be a cost effective substitute to std. Pt based CE and also opens up the possibility for the commercialization of DSSCs.

Acknowledgments

One of the authors, Dr.AS thanks the Pondicherry University for the financial support under Start-up Research Grant (Ref. No. PU/PC/start-up/2011-12/310) and the authors thank the CIF of Pondicherry University for extending the instrumentation facilities.

References

1. B. O'Regan and M. Gratzel, *Nature,* 1991, **353,** 737-740.
2. M. K. Nazeeruddin, A. Kay, I. Rodicio, R. Humphry-Baker, E. Mueller, P. Liska, N. Vlachopoulos and M. Graetzel, *J. Am. Ceram. Soc.,* 1993, **115,** 6382-6390.
3. S. Mathew, A. Yella, P. Gao, R. Humphry-Baker, F. E. Curchod, N. Ashari-Astani, I. Tavernelli, U. Rothlisberger, K. Nazeeruddin and M. Grätzel, *Nat Chem.,* 2014, **6,** 242-247.
4. E. Olsen, G. Hagen and S. Eric Lindquist, *Sol. Energy Mater. Sol. Cells,* 2000, **63,** 267-273.
5. G. Hashmi, K. Miettunen, T. Peltola, J. Halme, I. Asghar, K. Aitola, M. Toivola and P. Lund, *Renew Sus Energ Rev.,* 2011, **15,** 3717-3732.
6. K. Saranya, M. Rameez and A. Subramania, *Eur. Polym. J.,* 2015, **66,** 207-227.
7. M. Wu, X. Lin, Y. Wang, L. Wang, W. Guo, D. Qi, X. Peng, A. Hagfeldt, M. Grätzel and T. Ma, *J. Am. Ceram. Soc.,* 2012, **134,** 3419-3428.
8. S. I. Cha, B. K. Koo, S. H. Seo and D. Y. Lee, *J. Mater. Chem.,* 2010, **20,** 659-662.
9. P. Srinivasu, S. P. Singh, A. Islam and L. Han, *Int J. Photoenergy,* 2011, **2011,** 757421-757426.
10. H. Wang and Y. H. Hu, *Energy Environ. Sci.,* 2012, **5,** 8182-8188.
11. S. P. Lim, A. Pandikumar, Y. S. Lim, N. M. Huang and H. N. Lim, *Sci. Rep.,* 2014, **5305-5311**.
12. S. Thomas, T. G. Deepak, G. S. Anjusree, T. A. Arun, S. V. Nair and A. S. Nair, *J. Mater. Chem A,* 2014, **2,** 4474-4490.
13. W. Kwon, J.-M. Kim and S.W. Rhee, *J. Mater. Chem. A,* 2013, **1,** 3202-3215.

14. L. Zhang, A. Aboagye, A. Kelkar, C. Lai and H. Fong, *J .Mater Sci.,* 2014, **49,** 463-480.

15. M. Inagaki, Y. Yang and F. Kang, *Adv. Mater.,* 2012, **24,** 2547-2566.

16. L. Feng, N. Xie and J. Zhong, *Materials,* 2014, **7,** 3919-3945.

17. X. Zhang, P. Suresh Kumar, V. Aravindan, H. H. Liu, J. Sundaramurthy, S. G. Mhaisalkar, H. M. Duong, S. Ramakrishna and S. Madhavi, *J. Phy. Chem. C,* 2012, **116**, 14780-14788.

18. X. Zhang, V. Thavasi, S. G. Mhaisalkar and S. Ramakrishna, *Nanoscale,* 2012, **4**, 1707-1716.

19. X. Zhang, H. Liu, S. Petnikota, S. Ramakrishna and H. J. Fan, *J. Mater Chem A,* 2014, **2**, 10835-10841.

20. X. Zhang, V. Aravindan, P. S. Kumar, H. Liu, J. Sundaramurthy, S. Ramakrishna and S. Madhavi, *Nanoscale*, 2013, **5**, 5973-5980.

21. P. Joshi, L. Zhang, Q. Chen, D. Galipeau, H. Fong and Q. Qiao, *ACS Appl. Mater. Interfaces,* 2010, **2,** 3572-3577.

22. S. Sigdel, A. Dubey, H. Elbohy, A. Aboagye, D. Galipeau, L. Zhang, H. Fong and Q. Qiao, *J. Mater. Chem. A,* 2014, **2,** 11448-11453.

23. P. Joshi, Z. Zhou, P. Poudel, A. Thapa, X.-F. Wu and Q. Qiao, *Nanoscale*, 2012, **4,** 5659-5664.

24. Y. Zhao, A. Thapa, Q. Feng, M. Xi, Q. Qiao and H. Fong, *Nanoscale,* 2013, **5,** 11742-11747.

25. N. A. M. Barakat, M. Shaheer Akhtar, A. Yousef, M. El-Newehy and H. Y. Kim, *Chem. Eng. J.,* 2012, **211–212,** 9-15.

26. A. Yousef, M. S. Akhtar, N. A. M. Barakat, M. Motlak, O. B. Yang and H. Y. Kim, *Electrochim. Acta,* 2013, **102,** 142-148.

27. C. Burda, X. Chen, R. Narayanan and M. A. El-Sayed, *Chem. Rev.,* 2005, **105,** 1025-1102.

28. G. Chieffi, C. Giordano, M. Antonietti and D. Esposito, *J. Mater. Chem. A,* 2014, **2,** 11591-11596.

29. S. Gurmen, B. Ebin, S. Stopić and B. Friedrich, *J. Alloys Compd.,* 2009, **480**, 529-533.

30. H. Bisht, H. T. Eun, A. Mehrtens and M. A. Aegerter, *Thin Solid Films,* 1999, **351,** 109-114.

31. K. Saranya, N. Sivasankar and A. Subramania, *RSC Advances,* 2014, **4,** 36226-36233.

32. A. R. S. Priya, A. Subramania, Y.-S. Jung and K. J. Kim, *Langmuir,* 2008, **24,** 9816-9819.

33. H. Wu, C. Qian, Y. Cao, P. Cao, W. Li, X. Zhang and X. Wei, *J. Phys. Chem. Solids,* 2010, **71,** 290-295.

34. H. Zhou, Q. Yu, Q. Peng, H. Wang, J. Chen and Y. Kuang, *Mater. Chem and Physics,* 2008, **110**, 434-439.

35. X. An, D. Shin, J. D. Ocon, J. K. Lee, Y.-i. Son and J. Lee, *Chin. J. Catalysis,* 2014, **35**, 891-895.

36. G. Veerappan, K. Bojan and S. W. Rhee, *ACS Appl. Mater. Interfaces,* 2011, **3,** 857-862.

37. W. J. Lee, E. Ramasamy, D. Y. Lee and J. S. Song, *ACS Appl. Mater. Interfaces,* 2009, **1,** 1145-1149.

38. T. V. Reshetenko, L. B. Avdeeva, Z. R. Ismagilov, V. V. Pushkarev, S. V. Cherepanova, A. L. Chuvilin and V. A. Likholobov, *Carbon,* 2003, **41**, 1605-1615.

39. K. Imoto, K. Takahashi, T. Yamaguchi, T. Komura, J. I. Nakamura and K. Murata, *Sol. Energy Mater. Sol. Cells,* 2003, **79,** 459-469.

40. X. Pan, K. Zhu, G. Ren, N. Islam, J. Warzywoda and Z. Fan, *J. Mater. Chem. A,* 2014, **2,** 12746-12753.

41. J. Jin, X. Zhang and T. He, *J. Phys. Chem C,* 2014, **118,** 24877-24883.

42. M. H. Yeh , L. Y. Lin , J.S. Su, Y. A. Leu, R. Vittal, C. L. Sun and K.C. Ho, *Chem Electro Chem,* 2014, **1,** 416-425.

43. Z. Tang, Q. Tang, J. Wu, Y. Li, Q. Liu, M. Zheng, Y. Xiao, G. Yue, M. Huang and J. Lin, *RSC Advances*, 2012, **2,** 5034-5037.

44. T. N. Murakami, S. Ito, Q. Wang, M. K. Nazeeruddin, T. Bessho, I. Cesar, P. Liska, R. Humphry-Baker, P. Comte, P. Péchy and M. Grätzel, *J. Electrochem. Soc.,* 2006, **153,** A2255-A2261.

45. S. H. Park, H. R. Jung, B. K. Kim and W.J. Lee, *J. Photochem. Photobiol., A,* 2012, **246,** 45-49.

46. X. Zheng, J. Deng, N. Wang, D. Deng, W. H. Zhang, X. Bao and C. Li, *Angew. Chem.,* 2014, **53,** 7023 -7027.

47. C.-W. Kung, H. W. Chen, C. Y. Lin, K. C. Huang, R. Vittal and K. C. Ho, *ACS nano,* 2012, **6,** 7016-7025.

48. S.H. Park, H.-R. Jung and W. J. Lee, *Electrochim. Acta,* 2013, **102,** 423-428.

49. G. Veerappan, W. Kwon and S.W. Rhee, *J. Power Sources,* 2011, **196,** 10798-10805.

50. Q. Wang, S. Ito, M. Grätzel, F. Fabregat-Santiago, I. Mora-Seró, J. Bisquert, T. Bessho and H. Imai, *J. Phys. Chem. B,* 2006, **110,** 25210-25221.